A Multi-Parameter Global Electron Density Model (GEDM) From GNSS Radio Occultation Data

Linlin Li, Shuanggen Jin, *Senior Member, IEEE*, and Liangliang Yuan

***Abstract*— The precise 3-D ionospheric electron density (IED) modeling is in general difficult due to costly and insufficient observations in the ionosphere. The Constellation Observing System for Meteorology, Ionosphere, and Climate (COSMIC) mission has provided a significant opportunity for estimating the IED profile during the past 15 years. In this article, a precise empirical 3-D global electron density model (GEDM) from COSMIC GNSS radio occultation (RO) data is developed based on Fourier expansion and principal component analysis (PCA) and evaluated with independent datasets. Each profile is described by five essential parameters: the mean scale height Hm, bottom and topside slopes of the scale height (a1 and a2), peak density of the F2 layer (NmF2), and height of the F2 layer peak density (hmF2). The GEDM model can provide IED at any local time (LT) (0–24 h), F10.7 (70–150 sfu), Kp (0–9), latitude (90°S–90°N), longitude (180°W–180°E), and altitude, especially in the F region. The model is validated by the incoherent scatter radar (ISR), International Reference Ionosphere (IRI)-2020, K-Band Ranging system (KBR) of the Gravity Recovery and Climate Experiment (GRACE), and the Global Ionospheric Map (GIM) TEC in 2010 and 2014. The results show that the GEDM model has preferable reliability and consistency with respect to the independent observations and the IRI-2020 model. The statistical error of the GEDM model is lower than that of the IRI-2020, particularly in the mid-latitude region. Furthermore, the GEDM model is capable of precisely capturing typical ionospheric features, such as the equatorial ionization anomaly (EIA), winter anomaly, and the annual anomaly.**

***Index Terms*— Empirical electron density model, Global Navigation Satellite System (GNSS), principal component analysis (PCA), radio occultation (RO).**

I. Introduction

THE ionospheric electron density (IED) is a vital parameter in the ionospheric investigation. The IED distribution in the ionosphere could impact radio signal propagation and reflection. The IED estimation and study are therefore essential for satellite navigation, radio transmission, and space weather forecasting, among other applications. By more accurately observing and simulating the IED distribution, we have the potential to enhance the performance of related technologies and systems and increase the reliability and utility of communication and navigation. This is significant for expanding the scope of space activities.

To observe IED, several technologies have been developed. For instance, incoherent scatter radars (ISRs) at Millstone Hill and Arecibo can measure electron temperature and IED concurrently [1]. The digital ionosonde emits radio waves that go through the ionosphere vertically at a specific frequency. The relationship between scattering reflection and frequency indicates that the greater the frequency is, the less refraction penetrates the ionosphere and the higher the reflection height is. A frequency graph is used to measure the critical frequency and virtual height of the ionospheric vertical gauge for calculating the plasma density at this height. However, all of the aforementioned technologies have limits due to their high cost and continental location. They are unable to observe the ionosphere globally and continuously in time. We can now monitor the ionospheric IED by using probes since the development of in situ detection. With the development of the Global Navigation Satellite System (GNSS), it can monitor ionospheric total electron content (TEC) and IED [2], e.g., GNSS radio occultation (RO) [3]. It successfully compensates for data gaps in areas such as the ocean. Numerous spacecrafts have been successfully launched with carrying GNSS RO receivers thus far, including the GPS/MET [3], the Fengyun (FY) series satellites [4], and the Constellation Observing System for Meteorology, Ionosphere, and Climate (COSMIC) [5]. Opportunities expand the growth and applications of GNSS RO technology in ionospheric studies. Global positioning system (GPS) satellites broadcast signals with an orbit about 20 000 km above Earth's surface. Low Earth orbit (LEO) satellites equipped with GPS RO receivers can receive RO signals and estimate the ionospheric IED distribution for ionospheric detection.

The global IED model study is a hot topic in most GNSS applications. Nowadays, ionospheric data assimilation [6], theoretical (see [7], [8], [9]), empirical (see [10], [11]), and machine learning (see [12], [13]) models are one of the main focuses for ionospheric models. Empirical models, such as the NeQuick models, International Reference Ionosphere (IRI), Neustrelitz Electron Density Model (NEDM), Klobuchar models, and others, are mostly based on empirical parameters and

Manuscript received 15 July 2024; revised 28 August 2024; accepted 3 September 2024. Date of publication 6 September 2024; date of current version 26 September 2024. This work was supported by the National Natural Science Foundation of China (NSFC) Project under Grant 12073012. *(Corresponding author: Shuanggen Jin.)*

Linlin Li is with Shanghai Astronomical Observatory, Chinese Academy of Sciences, Shanghai 200030, China, and also with the School of Astronomy and Space Science, University of Chinese Academy of Sciences, Beijing 100049, China (e-mail: lilinlin@shao.ac.cn).

Shuanggen Jin is with Shanghai Astronomical Observatory, Chinese Academy of Sciences, Shanghai 200030, China, and also with the School of Surveying and Land Information Engineering, Henan Polytechnic University, Jiaozuo 454003, China (e-mail: sgjin@shao.ac.cn).

Liangliang Yuan is with Shanghai Astronomical Observatory, Chinese Academy of Sciences, Shanghai 200030, China (e-mail: llyuan@shao.ac.cn).

Digital Object Identifier 10.1109/TGRS.2024.3455254

basic physical equations. On the other hand, when modeling extreme cases, the model errors increase drastically. Compared to empirical models, theoretical models have a more complex physics basis and require more processing time. By adding relevant information about the magnetosphere, atmosphere, sun, and geomagnetism, physical characteristics such as ionospheric ion temperature, electron density, and ion drift velocity are estimated numerically in these models. The accuracy of the models is dependent on the input parameters and also constrained by the adopted physics simplifications and numerical instabilities. Global Ionosphere Thermosphere Model (GITM), SAMI3, and Thermosphere Ionosphere Electrodynamics General Circulation Model (TIE-GCM) are well-known models but still subject to large uncertainty. As neural networks (NNs) were developed, more models, such as recurrent NN (RNN), convolutional NN (CNN), backpropagation (BP), and various fusion models, are being developed. They are statistical models of data, which were produced by imitating the information-transmission and information-analysis processes of brain neurons. Although there are certain advancements, difficulties persist due to the ionospheric complexity and unpredictability. More work is required.

The empirical model represents variations in the ionospheric climatology according to several observations through different mathematical formulations. It is an essential technique for studying ionospheric variations because it can distinguish unique contributions from multiple contributing sources [14]. An IED model known as TWIM was investigated by Tsai et al. [15] using the GPS RO data. Nevertheless, the model can scarcely be applied to the forecast application because it is quite basic and solely concentrates on the GPS RO data. The NmF2 and hmF2 were provided by an empirical Canadian high Arctic ionospheric model that was based on all available ionosonde and RO IED data [16]. Using a function of F10.7 and ionospheric index, this regional model simulated solar cycle variability and seasonal variability via a Fourier expansion. Furthermore, Gowtam et al. [17] constructed a worldwide 3-D ionospheric IED model based on ionosonde, topside sensors, and RO data. However, since these models used a constant scale height, they might be inaccurate in high-altitude regions. A global IED model was constructed using RO data collected by COSMIC, CHAMP, and GRACE between July 2006 and June 2017 [18]. However, this model did not consider the longitudinal variation. Afterward, Li et al. [19] built a COSMIC-based model that provides 3-D IED at any longitude (180°W–180°E), latitude (90°N–90°S), month, LT (0–24 h), and F10.7 (70–150 sfu), while Kp and several key space weather parameters are equally important in driving the empirical model.

The development of GNSS RO data, particularly the COSMIC-2 mission, provides denser IED data. In this study, the COSMIC-1 data from 2007 to 2018 (11 years) and COSMIC-2 data from 2019 to 2023 (four years) are used for establishing the 3-D global electron density model (GEDM) with considering mean scale height (Hm), bottom and topside slopes of the scale height (a1 and a2), maximum density of the F2 layer (NmF2), and height of the F2 layer maximum density (hmF2) based on Fourier expansion and principal component analysis (PCA). The F10.7 and Kp are introduced to drive the model. In the next section, the results are presented and compared with the IRI-2020 and other observational data such as ISR, GIM, GRACE-KBR, and ionosonde. Finally, the discussion and conclusion are given in Sections IV and V, respectively.

II. Data and Algorithms

A. Data Preprocessing

GNSS RO provides an important chance to probe and investigate the topside ionosphere and plasmasphere. On April 15, 2006, the COSMIC-1 mission was launched with six LEO satellites at a height of approximately 800 km and an orbit inclination of 72°. The onboard GPS receivers of COSMIC satellites are equipped with four GPS antennas to track observations, including the GPS RO for atmospheric/ionospheric sounding. As for the COSMIC-2 mission, six LEO satellites were launched in June 2019 with a 24° inclination at an altitude of approximately 550 km. The COSMIC Data Analysis Achieve Center (CDAAC) provides the atmospheric and ionospheric profile data.

In each profile, the Chapman-α function is utilized to match the data. The year, day of year (DOY), Universal Time (UT), hmF2, NmF2, a1, a2, and Hm are obtained first. Then, the unreliable parameters are removed according to the R2 calculated from the least-squares method. The reliable profiles should satisfy the criteria: 1) $10^3 <= \text{NmF2} <= 10^7$ cm^{-3}; 2) 180 <= hmF2 <= 600 km; and 3) 5 <= Hm <= 200 (Le et al. [20]). Third, the Kp and F10.7 are matched one-on-one with each profile data above.

Chapman function is one of the most widely used functions to describe the ionospheric profiles [21], [22], [23], apart from the exponential function, parabolic function, and Epstein function. A famous Chapman-α function can be expressed as follows [24]:

$$\text{IED} = \text{NmF2} \cdot \exp\left\{\frac{1}{2}\left[1 - z(h) - \exp(-z(h))\right]\right\} \quad (1)$$

$$z(h) = \frac{h - \text{hmF2}}{H(h)} \quad (2)$$

$$H(h) = \begin{cases} a_1(h - \text{hmF2}) + \text{Hm}, & h \geq \text{hmF2} \\ a_2(h - \text{hmF2}) + \text{Hm}, & h < \text{hmF2}. \end{cases} \quad (3)$$

The profile with the peak plasma density (NmF2), the peak height (hmF2), and scale height (H) is well expressed. Previous studies showed that the scale height was vital, especially for the topside IED [25]. Using different linear fitting methods in the upper and lower regions of hmF2 to calculate elevation can better describe the ionospheric profile.

The ionospheric scale height is an indispensable factor for calculating topside electron density. Topside scale height is directly related to plasma temperature structure, composition, and ionospheric dynamics, and it has several practical applications [26]. There are three primary techniques to characterize ionospheric scale height: function-based effective scale height (ESH), vertical scale height (VSH), and plasma scale height (Hp). In addition, ESH is described as the scale height used to fit the IED profile using mathematical functions

such as the Epstein, Chapman, exponential, and parabolic functions according to a number of studies [22], [27], [28], [29]. The most popular ESH, alpha-Chapman scale height (Hm), is produced by fitting profiles using the Chapman-α function. To accurately represent the complex fluctuation of IED, Hm fluctuates with the height.

Different indices, such as Ap, Dst, and sunspot number (SSN), are available for solar and geomagnetic activity. However, according to recent results from previous machine learning, the Kp and F10.7 have more relatively complete descriptions for modeling. F10.7 is the degree of solar radio flux. The solar flux measurement value is determined by measuring the intensity of solar radio emission in a 100-MHz bandwidth centered on 1 h at 2800 MHz. Solar flux units (sfu) are employed, with one sfu equal to 10^{-22} W m^{-2} Hz^{-1}. Low solar activity is defined as F10.7 less than 100. It is believed that the solar is active if F10.7 is greater than 150. The change in one solar period, which is computed as follows, can be appropriately represented by the F10.7p, according to earlier studies [30], [31]

$$\mathrm{F10.7p} = \frac{\mathrm{F10.7\,A} + \mathrm{F10.7}}{2} \tag{4}$$

where F10.7 A is the 81-day moving average of the F10.7 index.

The irregular systems cause the variation in the geomagnetic field. K-index is a vital quasi-logarithmic local index of magnetic activity over three hours for a single geomagnetic observatory station. Here, the Kp index is used to represent variations in IED due to geomagnetic activity. This quantity is derived from 13 geomagnetic stations located in the geomagnetic coordinate system between 44°N and 60°S. Also, the index uses a single digit, 0–9, to represent each of the three hours of universal time in a day.

F10.7p, Kp, and COSMIC data utilization rates are shown in Fig. 1.

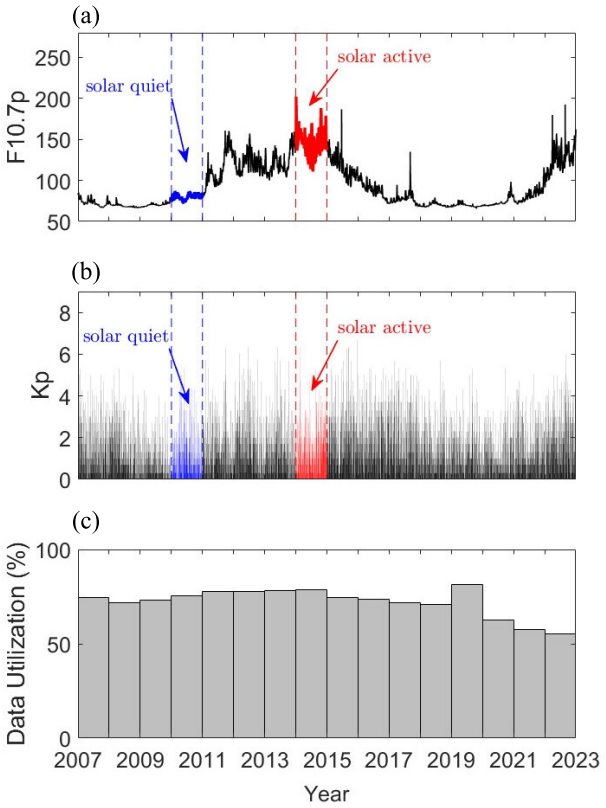

Fig. 1. (a) F10.7p, (b) Kp, and (c) COSMIC data utilization rate from 2007 to 2022. The blue and red parts represent the solar quiet and active periods chosen in the study, respectively.

B. Reconstruction Method

All the parameters are divided into 12 by the month and divided equally into 25 parts by the longitude. Then, there are 12 × 25 blocks. In each block, the spherical-harmonic basis function is used to fit. Taking NmF2 as an example, the NmF2 can be expressed as follows:

$$\begin{aligned}&\mathrm{NmF2(lat, LT, F10.7p, Kp)}\\&= \sum_{n=0}^{N}\sum_{m=0}^{n} P_n^m\left[\cos\left(\frac{\pi}{2} - \mathrm{lat}\right)\right]\left[C_{nm}\cos\left(m\cdot 2\pi\cdot\frac{\mathrm{LT}}{24}\right)\right.\\&\qquad\left. + S_{nm}\sin\left(m\cdot 2\pi\cdot\frac{LT}{24}\right)\right]\end{aligned} \tag{5}$$

$$C_{nm} = f_{nm} + f_{nm}^{'}\mathrm{F10.7p} + f_{nm}^{''}\mathrm{F10.7p^2} + f_{nm}^{'''}\mathrm{Kp} + f_{nm}^{''''}\mathrm{Kp^2} \tag{6}$$

$$S_{nm} = g_{nm} + g_{nm}^{'}\mathrm{F10.7p} + g_{nm}^{''}\mathrm{F10.7p^2} + g_{nm}^{'''}\mathrm{Kp} + g_{nm}^{''''}\mathrm{Kp^2} \tag{7}$$

where lat is the geophysical latitude, LT is the local time (LT), and F10.7p and Kp are matched indexes for each NmF2. f and g are the coefficients for each block. Besides, the order is 12 for the precise description of the parameters. Also, it is not hard to use these coefficients to rebuild a 5-D grid: NmF2 (latitude, longitude, LT, F10.7p, and Kp).

C. Model Parameter Acquisition

The PCA is a mathematical method for reducing the dimension of data [32]. The primary idea behind this method is to transfer original n-dimensional characteristics into k-dimensional orthogonal features, which are named principal components [19], [33]. The detailed steps are as follows. For a block, firstly, it normalizes it. To preserve more than 90% of the features, our principal component fraction is set to 4 with PCA.

When performing PCA to NmF2, the Fourier expansion is also applied, and the model coefficients are given as follows:

$$\begin{aligned}&A_k(\mathrm{month, F10.7p, Kp})\\&= \sum_{m=0}^{3}\left[\left(b_{k,m}\cdot\mathrm{F10.7p^2} + c_{k,m}\cdot\mathrm{F10.7p} + d_{k,m}\cdot\mathrm{Kp^2} + e_{k,m}\right.\right.\\&\qquad\left.\left.\cdot\mathrm{Kp} + f_{k,m}\right)\cdot\cos\left(\frac{2\pi\cdot\mathrm{month}\cdot m}{12}\right)\right]\\&+ \sum_{m=0}^{3}\left[\left(g_{k,m}\cdot\mathrm{F10.7p^2} + h_{k,m}\cdot F10.7p + j_{k,m}\cdot\mathrm{Kp^2} + l_{k,m}\right.\right.\\&\qquad\left.\left.\cdot\mathrm{Kp} + p_{k,m}\right)\cdot\sin\left(\frac{2\pi\cdot\mathrm{month}\cdot m}{12}\right)\right].\end{aligned} \tag{8}$$

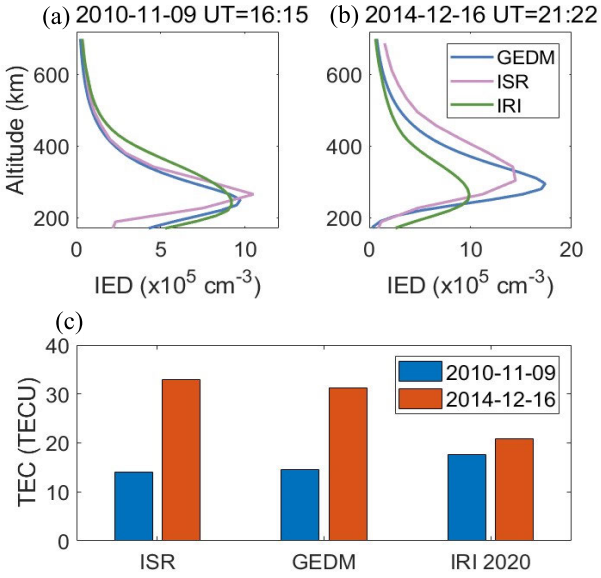

Fig. 2. One day IED from GEDM, Arecibo ISR, and IRI-2020 and the TEC comparison (c) in solar quiet year (a) and solar active year (b), respectively.

After all the steps are prepared, a series of coefficients are listed for calculating the model parameters. With these coefficients, the five parameters (NmF2, hmF2, a1, a2, and Hm) could be calculated for specific LT, month, F10.7, Kp, latitude, longitude, and altitude, and IED for further application is calculated with (1)–(3).

III. Results and Validation

2010 and 2014 are the solar and geomagnetic quiet and active years, as shown in Fig. 1, respectively. The GDEM results are obtained and validated by different observation results and models.

A. Comparison With ISR and IRI

2010-11-09 and 2014-12-16 are randomly chosen in solar quiet and solar active years, respectively. The IED profiles are obtained from ISR, IRI, and GEDM in Fig. 2. The IED from ISR is taken to be the reference value. At UT = 16:15, November 9, 2010, NmF2 is 1.325×10^6, 1.050×10^6, and 0.919×10^6 cm^{-3} for GEDM, ISR, and IRI-2020, and hmF2 is around 239, 265.2, and 235 km for GEDM, ISR, and IRI-2020. On 2014-12-16, UT = 21:22, NmF2 is 1.739×10^6, 1.445×10^6, and 0.988×10^6 cm^{-3} for GEDM, ISR, and IRI-2020, and hmF2 is around 295, 303.6, and 265 km for GEDM, ISR, and IRI-2020. The TEC is also calculated between 200 and 700 km, and the results are shown in Fig. 2(c). It is also found that the IRI-2020 usually underestimates the IED. On 2010-11-09, the TEC is 17.7 TECU, 14.6 TECU, and 14.0 TECU for IRI-2020, GEDM, and ISR, respectively, and the estimated TEC is 20.9 TECU, 31.3 TECU, and 32.9 TECU for IRI-2020, GEDM, and ISR on 2014-12-16. The GEDM result is the closest to the ISR results among others. In all, it is obviously noticed that the IED from GEDM shows good consistency with no matter observation data or other empirical models.

ISRs provide fairly accurate electron density data, and they can probe the whole electron density profile in the F region.

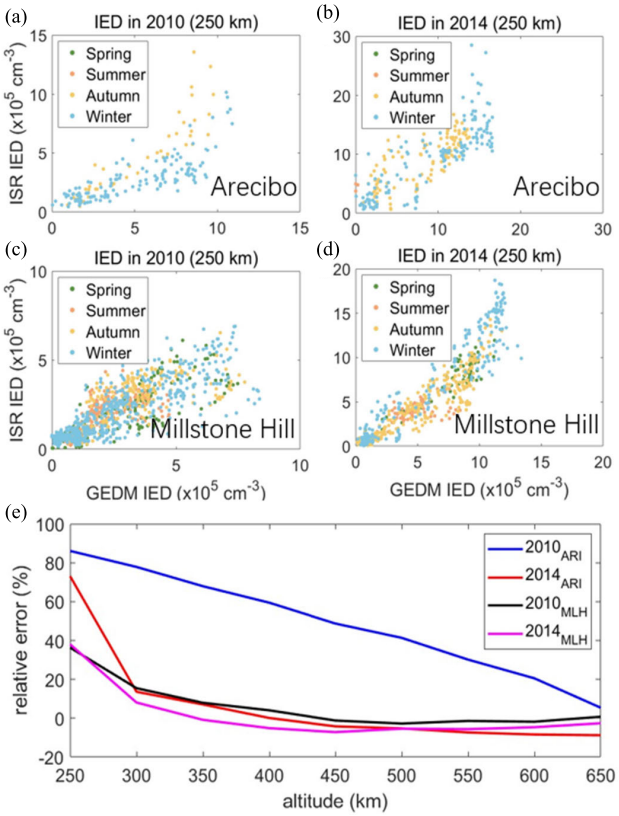

Fig. 3. Comparison of IED in four seasons between ISR and GEDM at Arecibo in 2010 (a) and 2014 (b), and Millstone Hill in 2010 (c) and 2014 (d). The relative error is shown in (e) from 250 to 650 km.

Fig. 3 shows the IED from Arecibo ISR (18.345°N and 66.75°W) [Fig. 3(a) and (b)] and Millstone Hill (42.62°N and 71.49°W) [Fig. 3(c) and (d)] compared with the model data in different solar activity years and seasons at around 250 km. Although the IEDs in spring and summer are rare in Arecibo, the correlation coefficients could be calculated, which are 0.71 and 0.80 at around 250 km in 2010 and 2014, respectively. For the Millstone Hill ISR, the correlation coefficients are 0.79 and 0.92. The results indicate that in solar active years in the mid-latitude region, the GEDM results are more coherent with the ISR. The relative error for the two ISRs in various heights, ranging from 250 to 650 km, is provided in Fig. 3(e). The relative error decreases with height, demonstrating how the accuracy of COSMIC RO data varies with altitude, which is related to the occultation algorithm. In addition, the mid-latitude region has less error than the low-latitude region. It is evident that the GEDM performs better in mid latitudes.

B. Annual TEC Variations

The TEC is calculated for further comparison. The global ionospheric map (GIM) from CAS (ftp://ftp.gipp.org.cn/product/ionex/) is used as the reference. The GEDM TEC is obtained with the integral method.

Fig. 4 gives out the daily average TEC from the GIM, GEDM, and IRI-2020 in 2010 and 2014. The TEC from the GEDM and IRI-2020 are lower than the reference no matter in 2010 and 2014. Compared with the IRI-2020 results, the GEDM is closer to the GIM data, which means that the GEDM

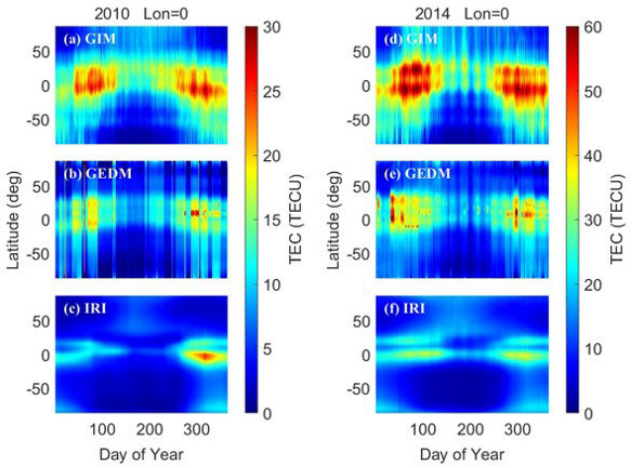

Fig. 4. Daily TEC from GIM, GEDM, and IRI-2020 in 2010 (left panel) and 2014 (right panel). (a) GIM. (b) GEDM. (c) IRI.

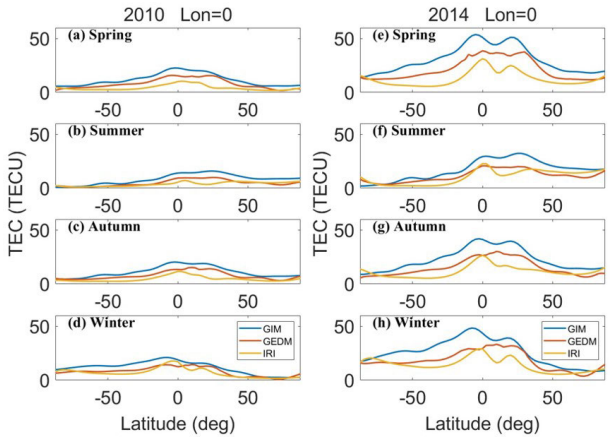

Fig. 5. Average daily TEC in different seasons in 2010 (left panel) and 2014 (right panel). (a)–(d) spring, summer, autumn, and winter in 2010. (e)–(h) spring, summer, autumn, and winter in 2010.

can estimate the TEC better. In 2014, the IRI-2020 TEC in mid- to low-latitude regions was less than half of the GIM, which shows that the IRI-2020 could cause great errors when computing the TEC.

Fig. 5 shows the average TEC in different seasons. When considering the seasons, we refer to the northern hemisphere. Overall, the TEC from the GEDM is between the GIM and IRI. All of the GIM TEC are higher than the estimation results from the GEDM and IRI-2020 because GIM TEC is calculated from the GPS height to the ground, while the TEC from the IRI and the GEDM is calculated from the ground to LEO height. The TEC has two peaks in both hemispheres, which are concentrated between mid- and low-latitude regions. It can also be found that the GEDM shows three TEC peaks, while the others show two peaks. The different peak is located around 10°N, which is near the magnetic equator, indicating a larger region. As is known, the profiles from COSMIC have a greater error in the magnetic equator region because of the IED distribution. The TEC varies in different seasons. The mean error is greater in the spring and 2014. The TEC estimated by IRI and GEDM is more consistent. More details are listed in Table I.

TABLE I
MEAN TEC ERROR SUMMARY IN 2010 AND 2014

Season	Error (TECU)	2010	2014
Spring	GIM-GEDM	3.64	9.23
	GIM-IRI	7.43	17.74
	GEDM-IRI	3.79	8.51
Summer	GIM-GEDM	3.56	5.55
	GIM-IRI	4.60	6.59
	GEDM-IRI	1.05	1.03
Autumn	GIM-GEDM	3.34	7.50
	GIM-IRI	6.49	11.27
	IRI-GEDM	3.15	3.77
Winter	GIM-GEDM	3.61	7.60
	GIM-IRI	4.74	11.69
	GEDM-IRI	1.13	4.09

In general, both the GEDM and IRI-2020 underestimated TEC, as the electron density from the plasmasphere was not precisely included in the calculation. The GEDM better computes the TEC than IRI-2020 in the F region.

C. Topside IED Comparison

In 2002, two co-orbiting Gravity Recovery and Climate Experiment (GRACE) mission satellites were launched mainly for the Earth's gravity field temporal variations detection with an initial altitude of about 490 km. In this section, the IED observation data are not only from the COSMIC data but also measured by the GRACE K-Band Ranging System (KBR). The range difference between the two GRACE satellites can be accurately measured by the KBR system. The differential TEC obtained from the range variation between the two satellites was used to estimate the average electron densities [35]. Xiong et al. [36] evaluated the quality of the KBR electron densities and discovered that the KBR-estimated densities agreed with ISR data from Arecibo, Millstone Hill, Jicamarca, and EISCAT.

Fig. 6 shows a global IED comparison between GRACE-KBR, GEDM, and IRI at 470 km in 2010. The GRACE-KBR IED is assumed as the reference.

Fig. 7 shows the global IED comparison between GRACE-KBR, GEDM, and IRI at 425 km in 2014. Relative errors are shown in Figs. 8 and 9. Substantially, the IED is consistent with the GRACE-KBR, GEDM, and IRI-2020. For 2010, the GEDM overestimated IED in the northern hemisphere.

Although both the GEDM and IRI-2020 underestimate IED in low-latitude regions, especially in winter, the GEDM underestimates IED even more than in other seasons, which can run to more than -2×10^5 cm^{-3}. In the low-latitude regions of 2014, the GEDM overestimated IED at certain latitudes, which can reach 5×10^5 cm^{-3}. This model outperforms IRI-2020 in estimating the top ionospheric IED. It is obvious that the IRI-2020 always overestimates the IED and the estimation error of the IRI is greater than that of the GEDM in the southern hemisphere. As is known to all, the IRI-2020 is not only based on space-based instruments but also on ground-based detectors. Due to the influence of terrain, the number of ground-based detectors in the southern hemisphere

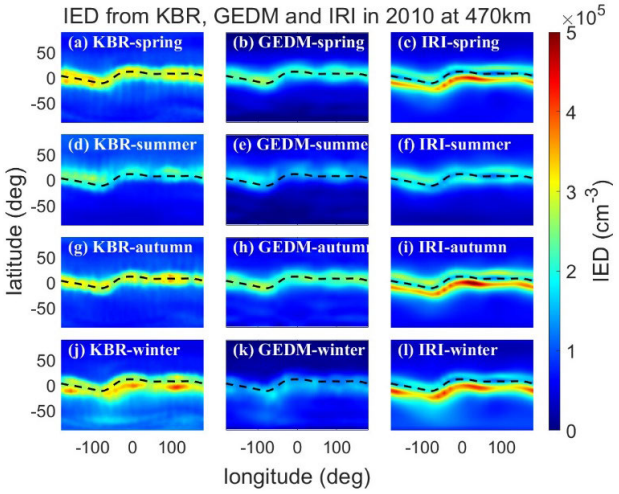

Fig. 6. Global IED comparison between GRACE-KBR, GEDM, and IRI at 470 km in 2010. The dashed line is the magnetic equator. (a) KBR-spring. (b) GEDM-spring. (c) IRI-spring. (d) KBR-summer. (e) GEDM-summer. (f) IRI-summer. (g) KBR-autumn. (h) GEDM-autumn. (i) IRI-autumn. (j) KBR-winter. (k) GEDM-winter. (l) IRI-winter.

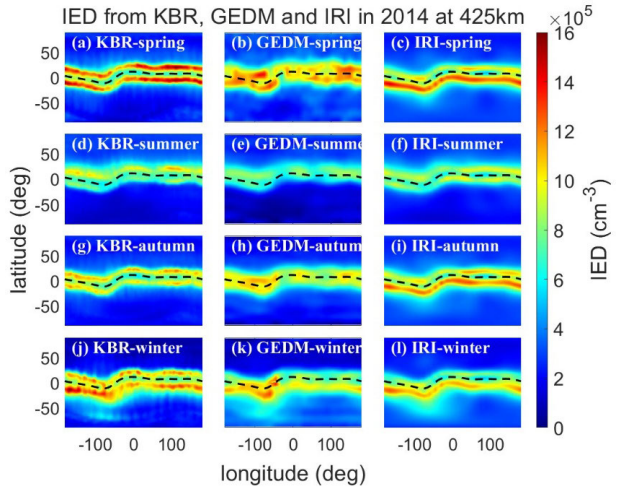

Fig. 7. Global IED comparison between GRACE-KBR, GEDM, and IRI at 425 km in 2014. The dashed line is the magnetic equator. (a) KBR-spring. (b) GEDM-spring. (c) IRI-spring. (d) KBR-summer. (e) GEDM-summer. (f) IRI-summer. (g) KBR-autumn. (h) GEDM-autumn. (i) IRI-autumn. (j) KBR-winter. (k) GEDM-winter. (l) IRI-winter.

is relatively small. Therefore, in the southern hemisphere, compared to GEDM based on COSMIC, the greater error between IRI and the reference value is easily understood.

On the whole, the GEDM performs better in the topside IED estimation than IRI-2020. It has higher accuracy in mid-latitude regions, and the IED estimates are more accurate in summer.

D. hmF2 Comparison

The ionosonde is currently one of the main conventional instruments for ground vertical detection of the ionosphere. It obtains the ionospheric virtual height at each frequency point by measuring the time delay of the reflected echo from the ionosphere to the receiver.

We chose ionosonde stations with hmF2 data in 2010 and 2014, and the results are shown in Fig. 10. The correlation coefficients are 0.4, 0.8, 0.4, and 0.7, 2010, in different

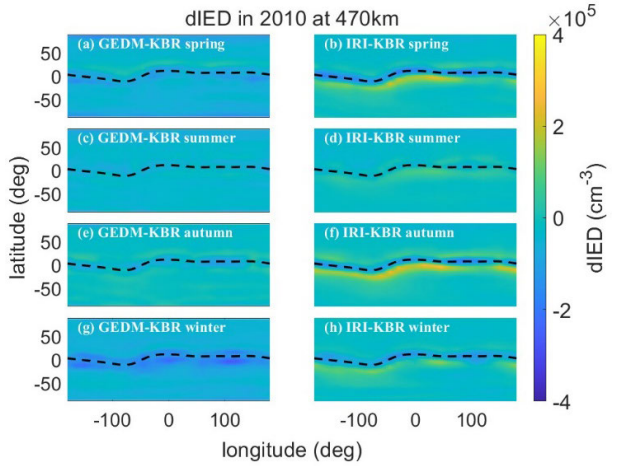

Fig. 8. Error between GRACE-KBR, GEDM, and IRI at 470 km in 2010. The dashed line is the magnetic equator. (a) GEDM-KBR spring. (b) IRI-KBR spring. (c) GEDM-KBR summer. (d) IRI-KBR summer. (e) GEDM-KBR autumn. (f) IRI-KBR autumn. (g) GEDM-KBR winter. (h) IRI-KBR winter.

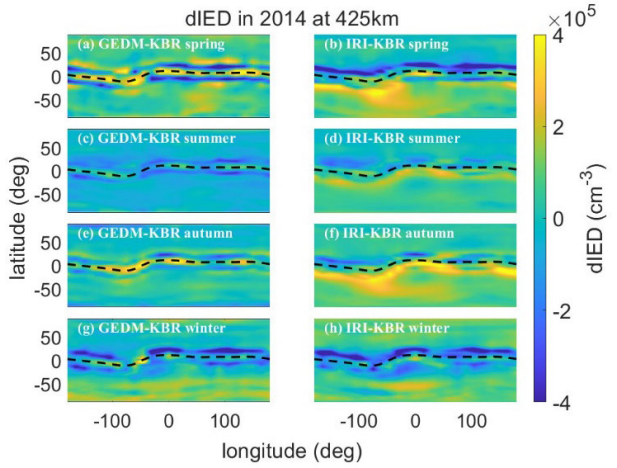

Fig. 9. Error between GRACE-KBR, GEDM, and IRI at 425 km in 2014. The dashed line is the magnetic equator. (a) GEDM-KBR spring. (b) IRI-KBR spring. (c) GEDM-KBR summer. (d) IRI-KBR summer. (e) GEDM-KBR autumn. (f) IRI-KBR autumn. (g) GEDM-KBR winter. (h) IRI-KBR winter.

seasons, and 0.5, 0.9, 0.7, and 0.8, 2014, in the four seasons. The coefficient is lower at the equinox than solstice. It was also larger in 2014. This means that the estimated hmF2 from the GEDM is more accordant with the ionosonde observation data in solar active years and solstice periods, which are similar to the ISR results before. Besides, the coefficients are different from each station. It is known that hmF2 from the ionosonde has measurement error because the height resolution of different ionosonde is not always uniform. It influences the correlation coefficients.

E. IED Profile Comparison

For 2010, the profile comparison among COSMIC, GEDM, and IRI-2020 results is shown in Fig. 11. The error between GEDM and IRI-2020 is presented in Fig. 12. A similar comparison for 2014 and error are shown in Figs. 13 and 14, respectively.

The GEDM is consistent with the results from the IRI-2020. The equatorial ionization anomaly (EIA) [34] is shown as two peaks at roughly $\pm 15^\circ$ latitude on either side of the equator.

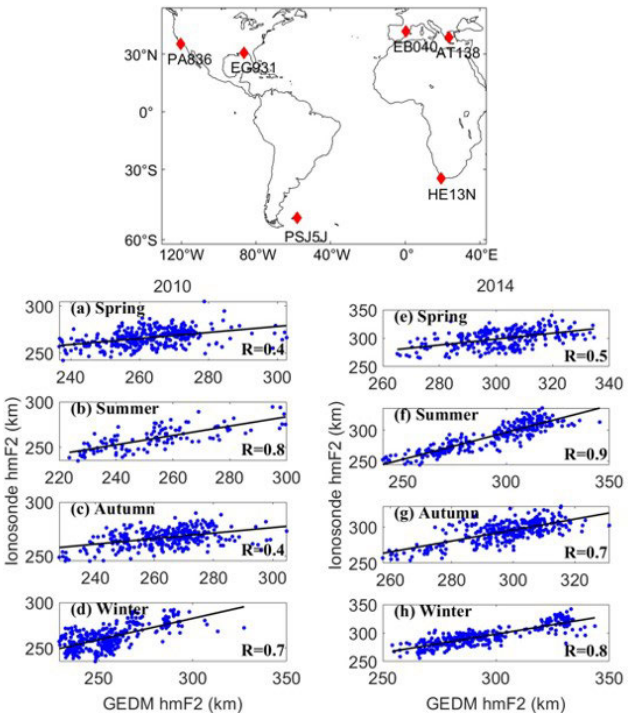

Fig. 10. Ionosonde stations and hmF2 from Ionosonde and GEDM in 2010 and 2014, respectively. (a)–(d) spring, summer, autumn, and winter in 2010. (e)–(h) are spring, summer, autumn, and winter in 2014.

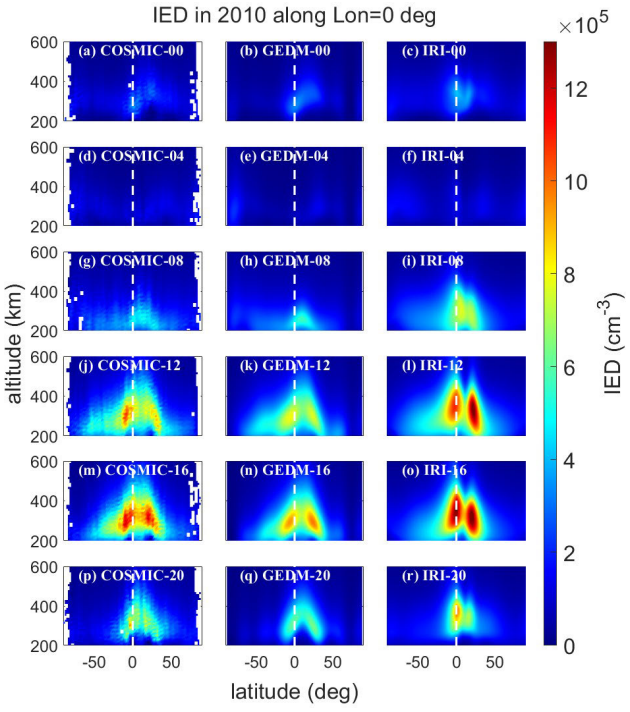

Fig. 11. IED profile comparison among COSMIC data, GEDM, and IRI in 2010. The white dashed line is the geomagnetic equator. The blank section is because of missing data. (a) COSMIC-00. (b) GEDM-00. (c) IRI-00. (d) COSMIC-04. (e) GEDM-04. (f) IRI-04. (g) COSMIC-08. (h) GEDM-08. (i) IRI-08. (j) COSMIC-12. (k) GEDM-12. (l) IRI-12. (m) COSMIC-16. (n) GEDM-16. (o) IRI-16. (p) COSMIC-20. (q) GEDM-20. (r) IRI-20.

The ionosphere is lifted and the plasma drifted upward due to the south–north magnetic field B and the eastward electric field E. Because of the differing densities at different heights, the plasma moved to the northern and southern hemispheres and

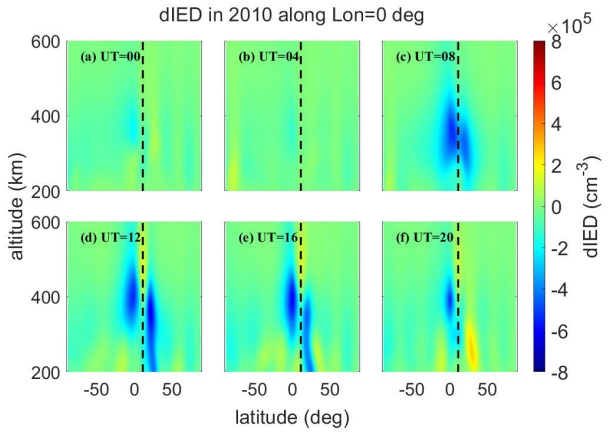

Fig. 12. Error distribution between GEDM and IRI in 2010. The black dashed line is the geomagnetic equator. (a) UT = 100. (b) UT = 04. (c) UT = 08. (d) UT = 12. (e) UT = 16. (f) UT = 20.

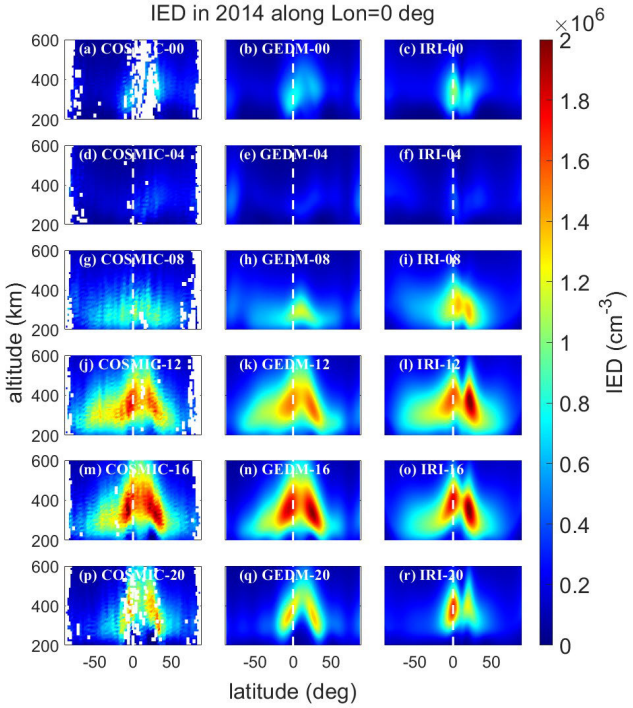

Fig. 13. IED profile comparison among COSMIC data, GEDM, and IRI in 2014. The white dashed line is the geomagnetic equator. The blank section is because of missing data. (a) COSMIC-00. (b) GEDM-00. (c) IRI-00. (d) COSMIC-04. (e) GEDM-04. (f) IRI-04. (g) COSMIC-08. (h) GEDM-08. (i) IRI-08. (j) COSMIC-12. (k) GEDM-12. (l) IRI-12. (m) COSMIC-16. (n) GEDM-16. (o) IRI-16. (p) COSMIC-20. (q) GEDM-20. (r) IRI-20.

was decreased as a result of gravity and the pressure gradient force.

In 2014, the IED was higher than in 2010, with the highest electron density occurring in the afternoon. From a height perspective, hmF2 in the southern hemisphere is slightly higher than that in the northern hemisphere. The main error in 2010 is between the geomagnetic equator after sunrise, which can reach around -6×10^5 cm^{-3} between 300 and 500 km. Also, the error reaches its minimum at noon. In 2014, the GEDM IED was greatly larger than the IRI-2020 IED above 400 km after UT = 12. The GEDM underestimates the IED at UT = 8 in the F region, which can reach 6×10^5 cm^{-3}. Also, the GEDM underestimates the IED at UT = 8 in

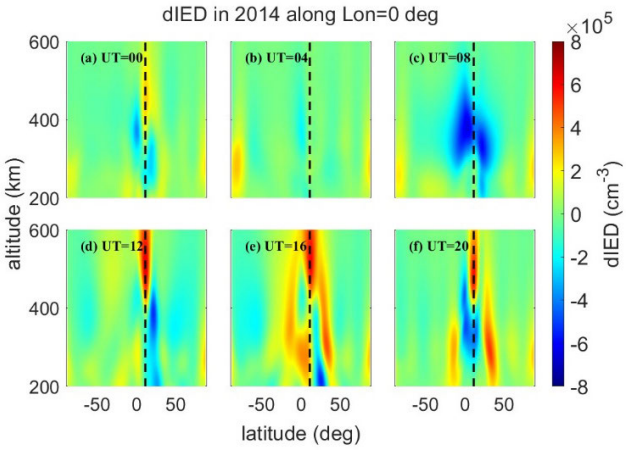

Fig. 14. Error distribution between GEDM and IRI in 2014. The black dashed line is the geomagnetic equator. (a) UT = 00. (b) UT = 04. (c) UT = 08. (d) UT = 12. (e) UT = 16. (f) UT = 20.

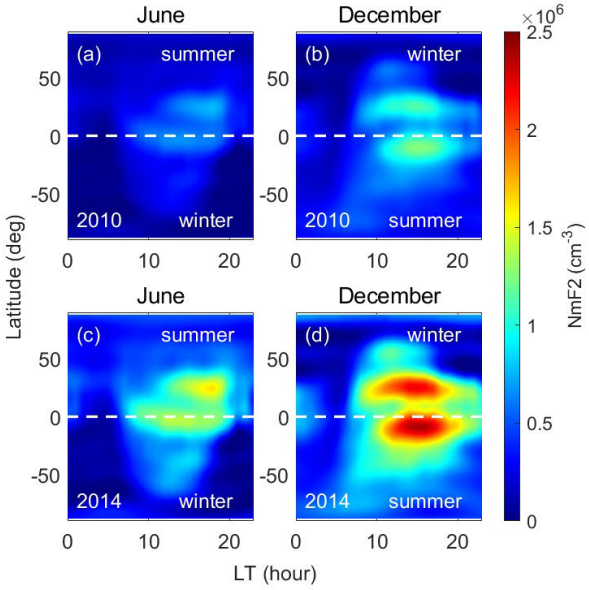

Fig. 15. Zonally averaged NmF2 during (a) June in 2010, (b) December in 2010, (c) June in 2014, and (d) December in 2014. The white dashed line represents the geographical equator.

the F region in both hemispheres, which can reach 6×10^5 cm^{-3}. Without the solar influence, the estimated IED is more accurate. The error in mid latitudes is less than in low-latitude regions, and it is also less in the solar quiet years. hmF2 is lower in the northern hemisphere. From 12 UT to 20 UT, the GEDM and observations experience bimodal merging. However, in IRI-2020, bimodal fusion was not demonstrated.

In all, the GEDM can capture the EIA, and bimodal fusion is well expressed.

IV. Discussion

The GEDM works well from the mid- to low-latitude regions because it can effectively capture EIA features, as demonstrated in Section III. As noted by earlier research, the two peaks can merge into one at higher altitudes such as Figs. 11 and 12 [5], [37]. However, the IRI-2020 is not able to well reproduce this phenomenon. In addition, it exhibits hemispheric asymmetry during solstices, which is likely related to the meridional wind effect. At noon or afternoon LT during the solstices, the higher peak initially appears in the south (north) hemisphere during winter (summer) and then moves to the north (south) hemisphere during summer (winter). The latitude, height, longitude, LT, and season of the EIA characteristics differ. Furthermore, the bimodal asymmetry agrees with the physical mechanisms that have been identified [38], [39], [40]. A powerful cross-equatorial neutral wind that flows from summer to winter is the cause of the asymmetry of hmF2. Meanwhile, it causes the plasma to go downward in the southern hemisphere and upward along magnetic field lines in the F region of the northern hemisphere. Before and after the solstice, strong winds blow from the summer to the winter hemisphere. The wind moves from the southern to the northern hemisphere around the winter solstice. The asymmetric structure of hmF2 is also shown in GEDM. The components of these winds aligned to the magnetic field push the F2 peak lower in the winter hemisphere close to the geomagnetic equator and carry a partially ionized atmosphere rising in the summer hemisphere. The fountain effect at the summer peak diminishes and the accumulation of plasma volume in the winter hemisphere is increased by the thermosphere circulation in the summer to winter hemisphere.

Winter and annual anomalies are also captured by the GEDM, which are depicted in Fig. 15. The NmF2 averages for June and December in the years 2010 and 2014 are noted. There is an annual anomaly present since the NmF2 in December is much higher than it is in June. In addition, NmF2 in the corresponding winter hemispheres is higher than that in the summer hemispheres between the morning and the noon, suggesting the occurrence of a winter anomaly. Furthermore, the winter anomaly is essentially nonexistent at mid-to-high-latitude regions. In the northern hemisphere's winter and solar active year, this effect is particularly noticeable. The change of the neutral composition is the main factor of the winter anomaly. Due to the atmospheric circulation between the two hemispheres [41], the related O/N_2 is decreased in the summer hemisphere and then increased in the other hemisphere.

For the top ionosphere, as shown in the comparison with the GRACE-KBR the GEDM outperforms the IRI-2020 imitation of IED, which is of great significance for future applications. Also, it has higher accuracy in mid latitudes, especially in summer.

The relative errors of two ISRs are displayed in Fig. 3(e). The COSMIC RO data are more precise at higher altitudes. When obtaining the IED profile through GNSS RO, the spherical symmetry is assumed. Thus, the horizontal gradient fluctuations of IED are ignored. There are large changes in IEDs along the boundary of EIA and in low-latitude areas with frequent plasma irregularities, resulting in a decrease in the precision of the IED profile from GNSS RO observations in this region. This might lead to a larger error for the Arecibo than Millstone Hill. In 2014, the EIA region widened in latitude, which can cover the Arecibo. Therefore, the inaccuracy in 2014 is less than in 2010 in Arecibo. There

are still some shortcomings in the GEDM, which need to be further optimized. For example, the simulation accuracy for low-latitude regions also needs to be further improved. Besides, higher resolution is required.

V. Conclusion

In this study, an empirical 3-D ionospheric model named the GEDM is constructed using the COSMIC GNSS RO data. The model is driven by F10.7 and Kp. The main conclusions and findings are summarized as follows.

1) The GEDM agrees well with the reference data from no matter observation data or IRI-2020 in the F region, especially in the mid-latitude region and solar active years.
2) Above 400 km, the IED is consistent among GRACE-KBR, GEDM, and IRI-2020, while the GEDM has higher accuracy in summer in mid latitudes at the top of the ionosphere. The GEDM has higher accuracy in the southern hemisphere compared with the IRI-2020.
3) The average TEC differences between GEDM and GIM are 3.53 TECU and 7.47 TECU in 2010 and 2014, respectively. The IRI-2020 always underestimates the TEC, although it can precisely compute the TEC in the F region, which needs further improvement to simulate the IED on the topside of the ionosphere.
4) EIA, annual anomaly, and winter anomaly are well captured by the GEDM. However, the TEC estimation around 10°N has a little greater error. Also, asymmetric peaks on both sides of the equator have been seized. The EIA and the plasma irregularities have an impact on the IED from radio occultation, especially at low altitudes.

In all, the GEDM can help to analyze several aspects of the ionospheric climate, including regional structures, seasonal variations, and dependency on solar activity and geomagnetic fields. It could enhance the topside ionosphere TEC estimation, which is important from an engineering viewpoint. In the F region, the gridded data can serve as a background ionosphere for ionospheric data assimilations.

Acknowledgment

The authors would like to appreciate the SPDF (https://spdf.gsfc.nasa.gov/) for providing the F10.7 and Kp index. The ISR data from Arecibo and Millstone Hill are available via http://cedar.openmadrigal.org. The COSMIC profiles are supplied by the COSMIC Data Analysis and Archive Center (https://cdaac-www.cosmic.ucar.edu/) and Taiwan Analysis Center for COSMIC (https://tacc.cwb.gov.tw). The GIM data are from the CAS (ftp://ftp.gipp.org.cn/product/ionex/). The ionosonde data are downloaded from https://giro.uml.edu/. LY provides the GRACE-KBR measurement data. The IRI-2020 source code is from http://irimodel.org/.

References

[1] J. Lei, R. G. Roble, W. Wang, B. A. Emery, and S. Zhang, "Electron temperature climatology at Millstone Hill and Arecibo," *J. Geophys. Res., Space Phys.*, vol. 112, no. 2, Feb. 2007, Art. no. A02302, doi: 10.1029/2006ja012041.

[2] S. G. Jin, J. Wang, H. Zhang, and W. Y. Zhu, "Real-time monitoring and prediction of the total ionospheric electron content by means of GPS observations," *Chin. Astron. Astrophys.*, vol. 28, no. 3, pp. 331–337, 2004, doi: 10.1016/j.chinastron.2004.07.008.

[3] S. G. Jin et al., "Remote sensing and its applications using GNSS reflected signals: Advances and prospects," *Satell. Navigat.*, vol. 5, no. 1, 2024, Art. no. 19, doi: 10.1186/s43020-024-00139-4.

[4] J. Lei, S. Syndergaard, and A. G. Burns, "Comparison of COSMIC ionospheric measurements with ground-based observations and model predictions: Preliminary results," *J. Geophys. Res., Space Phys.*, vol. 112, no. 7, Jul. 2007, Art. no. A07308, doi: 10.1029/2006ja012240.

[5] C. H. Lin et al., "Motions of the equatorial ionization anomaly crests imaged by FORMOSAT-3/COSMIC," *Geophys. Res. Lett.*, vol. 34, no. 19, Oct. 2007, Art. no. L19101, doi: 10.1029/2007gl030741.

[6] M. J. Wu et al., "Data assimilation of plasmasphere and upper ionosphere using COSMIC/GPS slant TEC measurements," *Radio Sci.*, vol. 50, no. 11, pp. 1131–1140, Nov. 2015, doi: 10.1002/2015RS005732.

[7] R. E. Dickinson, E. C. Ridley, and R. G. Roble, "A three-dimensional general circulation model of the thermosphere," *J. Geophys. Res., Space Phys.*, vol. 86, no. 3, pp. 1499–1512, Mar. 1981, doi: 10.1029/ja086ia03p01499.

[8] A. J. Ridley, Y. Deng, and G. Tóth, "The global ionosphere–thermosphere model," *J. Atmos. Solar-Terr. Phys.*, vol. 68, no. 8, pp. 839–864, May 2006, doi: 10.1016/j.jastp.2006.01.008.

[9] J. Huba and J. Krall, "Modeling the plasmasphere with SAMI3," *Geophys. Res. Lett.*, vol. 40, no. 1, pp. 6–10, Jan. 2013, doi: 10.1029/2012gl054300.

[10] D. Bilitza, L.-A. McKinnell, B. Reinisch, and T. Fuller-Rowell, "The international reference ionosphere today and in the future," *J. Geodesy*, vol. 85, no. 12, pp. 909–920, Dec. 2011, doi: 10.1007/s00190-010-0427-x.

[11] M. Nigussie, S. M. Radicella, B. Damtie, E. Yizengaw, B. Nava, and L. Roininen, "Validation of NeQuick TEC data ingestion technique against C/NOFS and EISCAT electron density measurements," *Radio Sci.*, vol. 51, no. 7, pp. 905–917, Jul. 2016, doi: 10.1002/2015RS005930.

[12] G. K. Zewdie, C. Valladares, M. B. Cohen, D. J. Lary, D. Ramani, and G. M. Tsidu, "Data-Driven forecasting of low-latitude ionospheric total electron content using the random forest and LSTM machine learning methods," *Space Weather*, vol. 19, no. 6, Jun. 2021, Art. no. e2020SW002639, doi: 10.1029/2020sw002639.

[13] S. Dutta and M. B. Cohen, "Improving electron density predictions in the topside of the ionosphere using machine learning on in situ satellite data," *Space Weather*, vol. 20, no. 9, Sep. 2022, Art. no. e2022SW003134, doi: 10.1029/2022sw003134.

[14] J. L. Lean, R. R. Meier, J. M. Picone, F. Sassi, J. T. Emmert, and P. G. Richards, "Ionospheric total electron content: Spatial patterns of variability," *J. Geophys. Res., Space Phys.*, vol. 121, no. 10, pp. 10367–10402, Oct. 2016, doi: 10.1002/2016ja023210.

[15] L.-C. Tsai, C. H. Liu, T. Y. Hsiao, and J. Y. Huang, "A near real-time phenomenological model of ionospheric electron density based on GPS radio occultation data," *Radio Sci.*, vol. 44, no. 5, pp. 1–10, Oct. 2009, doi: 10.1029/2009RS004154.

[16] D. R. Themens, P. T. Jayachandran, I. Galkin, and C. Hall, "The empirical Canadian high Arctic ionospheric model (E-CHAIM):N_mF_2 and h_mF_2," *J. Geophys. Res., Space Phys.*, vol. 122, no. 8, pp. 9015–9031, Aug. 2017, doi: 10.1002/2017ja024398.

[17] V. S. Gowtam, S. Tulasi Ram, B. Reinisch, and A. Prajapati, "A new artificial neural network-based global three-dimensional ionospheric model (ANNIM-3D) using long-term ionospheric observations: Preliminary results," *J. Geophys. Res., Space Phys.*, vol. 124, no. 6, pp. 4639–4657, Jun. 2019, doi: 10.1029/2019ja026540.

[18] M.-L. Zhang, L. Liu, and Q. Li, "Modeling the global ionospheric electron densities based on the EOF decomposition of the ionospheric radio occultation observation," *Adv. Space Res.*, vol. 68, no. 5, pp. 2218–2232, Sep. 2021, doi: 10.1016/j.asr.2020.09.033.

[19] Q. Li et al., "A global empirical model of electron density profile in the F region ionosphere basing on COSMIC measurements," *Space Weather*, vol. 19, no. 4, Apr. 2021, Art. no. e2020SW002642, doi: 10.1029/2020sw002642.

[20] H. Le et al., "A new global ionospheric electron density model based on grid modeling method," *Space Weather*, vol 20, no. 6, 2022, Art. no. e2021SW002992, doi: 10.1029/2021SW002992.

[21] H. G. Booker, "Fitting of multi-region ionospheric profiles of electron density by a single analytic function of height," *J. Atmos. Terr. Phys.*, vol. 39, no. 5, pp. 619–623, May 1977, doi: 10.1016/0021-9169(77)90072-1.

[22] K. Rawer, "Synthesis of ionospheric electron density profiles with Epstein functions," *Adv. Space Res.*, vol. 8, no. 4, pp. 191–198, 1988, doi: 10.1016/0273-1177(88)90239-6.
[23] K. Rawer, D. Bilitza, and T. L. Gulyaeva, "New formulas for the IRI electron density profile in the topside and middle ionosphere," *Adv. Space Res.*, vol. 5, no. 7, pp. 3–12, Jan. 1985, doi: 10.1016/0273-1177(85)90347-3.
[24] L. Liu, M. He, W. Wan, and M. Zhang, "Topside ionospheric scale heights retrieved from constellation observing system for meteorology, ionosphere, and climate radio occultation measurements," *J. Geophys. Res., Space Phys.*, vol. 113, no. 10, Oct. 2008, Art. no. A10304, doi: 10.1029/2008ja013490.
[25] A. Belehaki, P. Marinov, I. Kutiev, N. Jakowski, and S. Stankov, "Comparison of the topside ionosphere scale height determined by topside sounders model and bottomside digisonde profiles," *Adv. Space Res.*, vol. 37, no. 5, pp. 963–966, Jan. 2006, doi: 10.1016/j.asr.2005.09.014.
[26] L. Liu, W. Wan, M. L. Zhang, B. Ning, S. R. Zhang, and J. M. Holt, "Variations of topside ionospheric scale heights over Millstone Hill during the 30-day incoherent scatter radar experiment," *Ann. Geophys.*, vol. 25, no. 9, pp. 2019–2027, 2007, doi: 10.5194/angeo-25-2019-2007.
[27] S. Chapman, "The absorption and dissociative or ionizing effect of monochromatic radiation in an atmosphere on a rotating Earth part II. Grazing incidence," *Proc. Phys. Soc.*, vol. 43, no. 5, pp. 483–501, Sep. 1931, doi: 10.1088/0959-5309/43/5/302.
[28] B. W. Reinisch, X.-Q. Huang, A. Belehaki, J.-K. Shi, M.-L. Zhang, and R. Ilma, "Modeling the IRI topside profile using scale heights from ground-based ionosonde measurements," *Adv. Space Res.*, vol. 34, no. 9, pp. 2026–2031, 2004, doi: 10.1016/j.asr.2004.06.012.
[29] K. Venkatesh, P. V. S. R. Rao, P. L. Saranya, D. S. V. V. D. Prasad, and K. Niranjan, "Vertical electron density and topside effective scale height (HT) variations over the Indian equatorial and low latitude stations," *Annales Geophy.*, vol. 29, no. 10, pp. 1861–1872, Oct. 2011, doi: 10.5194/angeo-29-1861-2011.
[30] L. Liu, W. Wan, B. Ning, O. M. Pirog, and V. I. Kurkin, "Solar activity variations of the ionospheric peak electron density," *J. Geophys. Res., Space Phys.*, vol. 111, no. 8, Aug. 2006, Art. no. A08304, doi: 10.1029/2006ja011598.
[31] R. Ma, J. Xu, W. Wang, and W. Yuan, "Seasonal and latitudinal differences of the saturation effect between ionospheric N_mF_2 and solar activity indices," *J. Geophys. Res., Space Phys.*, vol. 114, no. 10, Oct. 2009, Art. no. A10303, doi: 10.1029/2009ja014353.
[32] K. Pearson, "On lines and planes of closest fit to systems of points in space," *Philos. Mag.*, vol. 2, no. 6, pp. 559–572, 1901, doi: 10.1080/14786440109462720.
[33] H. Le, N. Yang, L. Liu, Y. Chen, and H. Zhang, "The latitudinal structure of nighttime ionospheric TEC and its empirical orthogonal functions model over North American sector," *J. Geophys. Res., Space Phys.*, vol. 122, no. 1, pp. 963–977, Jan. 2017, doi: 10.1002/2016ja023361.
[34] J. A. Bittencourt, V. G. Pillat, P. R. Fagundes, Y. Sahai, and A. A. Pimenta, "LION: A dynamic computer model for the low-latitude ionosphere," *Annales Geophysicae*, vol. 25, no. 11, pp. 2371–2392, Nov. 2007, doi: 10.5194/angeo-25-2371-2007.
[35] C. Xiong, H. Lühr, S. Ma, and K. Schlegel, "Validation of GRACE electron densities by incoherent scatter radar data and estimation of plasma scale height in the topside ionosphere," *Adv. Space Res.*, vol. 55, no. 8, pp. 2048–2057, Apr. 2015, doi: 10.1016/j.asr.2014.07.022.
[36] C. Xiong, H. Lühr, S. Ma, and K. Schlegel, "Validation of GRACE electron densities by incoherent scatter radar data and estimation of plasma scale height in the topside ionosphere," *Adv. Space Res.*, vol. 55, no. 8, pp. 2048–2057, Apr. 2015, doi: 10.1016/j.asr.2014.07.022.
[37] S. Tulasi Ram, S. Su, and C. H. Liu, "FORMOSAT-3/COSMIC observations of seasonal and longitudinal variations of equatorial ionization anomaly and its interhemispheric asymmetry during the solar minimum period," *J. Geophys. Res., Space Phys.*, vol. 114, no. 6, Jun. 2009, Art. no. A06311, doi: 10.1029/2008ja013880.
[38] L. Huang et al., "Analysis of the north–south asymmetry of the equatorial ionization anomaly around 110 E longitude," *J. Atmos. Solar-Terr. Phys.*, vol. 102, pp. 354–361, Sep. 2013, doi: 10.1016/j.jastp.2013.06.010.
[39] X. Luan, P. Wang, X. Dou, and Y. C. Liu, "Interhemispheric asymmetry of the equatorial ionization anomaly in solstices observed by COSMIC during 2007–2012," *J. Geophys. Res., Space Phys.*, vol. 120, no. 4, pp. 3059–3073, Apr. 2015, doi: 10.1002/2014ja020820.
[40] A. Loutfi et al., "Interhemispheric asymmetry of the equatorial ionization anomaly (EIA) on the African sector over 3 years (2014–2016): Effects of thermospheric meridional winds," *J. Geophys. Res., Space Phys.*, vol. 127, no. 9, Sep. 2022, Art. no. e2021JA029902, doi: 10.1029/2021ja029902.
[41] A. G. Burns et al., "On the solar cycle variation of the winter anomaly," *J. Geophys. Res., Space Phys.*, vol. 119, no. 6, pp. 4938–4949, Jun. 2014, doi: 10.1002/2013ja019552.

Linlin Li received the B.Sc. degree from the School of Astronomy and Space Science, Nanjing University, Nanjing, China, in 2021. She is currently pursuing the Ph.D. degree with Shanghai Astronomical Observatory, Chinese Academy of Sciences, Shanghai, China.

Her current research mainly focuses on space science and ionospheric modeling.

Shuanggen Jin (Senior Member, IEEE) received the B.Sc. degree in geodesy from Wuhan University, Wuhan, China, in 1999, and the Ph.D. degree in geodesy from the University of Chinese Academy of Sciences, Beijing, China, in 2003.

He is currently a Professor with Shanghai Astronomical Observatory, Chinese Academy of Sciences, Shanghai, China, and the Vice-President and a Professor at Henan Polytechnic University, Jiaozuo, China. He has published over 500 articles in peer-reviewed journals and conference proceedings, 30 patents/software copyrights, and 15 books/monographs with more than 15000 citations and an H-index of 65. His main research areas include satellite navigation, remote sensing, and space/planetary exploration.

Dr. Jin was an IAG Fellow; an IUGG Fellow; a fellow of the Electromagnetics Academy; a fellow of the African Academy of Sciences; the World Class Professor of the Ministry of Education and Cultures, Indonesia; the Chief Scientist of the National Key Research and Development Program, China; a member of Academia Europea; a member of the Russian Academy of Natural Sciences; a member of the European Academy of Sciences; and a member of Turkish Academy of Sciences. He was the President of the International Association of Planetary Sciences (IAPS) from 2015 to 2019, the President of the International Association of CPGPS from 2016 to 2017, the Chair of the IUGG Union Commission on Planetary Sciences (UCPS) from 2015 to 2023, the Editor-in-Chief of the *International Journal of Geosciences*, an Editor of the *Geoscience Letters*, an Associate Editor of IEEE TRANSACTION ON GEOSCIENCES AND REMOTE SENSING AND JOURNAL OF NAVIGATION, and an Editorial Board Member of *Remote Sensing*, *GPS Solutions*, and *Journal of Geodynamics*.

Liangliang Yuan received the B.Sc. degree from the School of Astronomy and Space Science, Nanjing University, Nanjing, China, in 2016, and the Ph.D. degree from the University of Chinese Academy of Sciences, Beijing, China, in 2020.

He is currently an Associate Professor with Shanghai Astronomical Observatory, Chinese Academy of Sciences, Shanghai, China. He has worked at German Aerospace Center as a Research Associate for more than three years. His current research areas include the GNSS ionosphere sounding, thermosphere–ionosphere modeling, and ionospheric data assimilation.